Automatic evaluation of the Valsalva sinuses from cine-MRI

Cédric Blanchard, Alain Lalande, Tadeusz Sliwa, Olivier Bouchot, Yvon Voisin

Automatic evaluation of the Valsalva sinuses from cine-MRI

Cédric Blanchard, Alain Lalande, Tadeusz Sliwa, Olivier Bouchot, Yvon Voisin

Abstract
Object Although, there is no global consensus on their measurement, magnetic resonance imaging (MRI) appears to be particularly attractive for the study of the sinuses of Valsalva (SV). The purpose of this study was to automatically evaluate the SV from cine-MRI using a standardized method.
Materials and methods An automatic method based on mathematical morphology was elaborated to segment the aortic root from cross-sectional cine-MRI, and to detect relevant points, such as the commissures, the cusps and the centre of the SV. The distances between these points allow a metric evaluation of the SV. Our method was tested on synthesized data and 41 patient data sets and radii calculations were compared with manual processing.
Results On the patient data sets, there are excellent correlation and concordance between manual and automatic measurements for images at diastole ($r = 0.97$; $y = 0.97x + 0.57$; $P < 10^{-5}$; mean of differences = 0.2 mm; standard deviation of differences = 2.0 mm) and at systole ($r = 0.96$; $y = 0.96x + 1.2$; $P < 10^{-5}$; mean of differences < 0.1 mm; standard deviation of differences = 2.4 mm).
Conclusion Our automatic method provides reliable morphometric evaluation of the SV. Measures of distances between relevant points allow a precise evaluation of each cusp of the SV. This robust evaluation can be helpful in the follow-up of patients with aortic root diseases.

Keywords Sinus of Valsalva · Image processing · Computer-assisted · Automatic data processing · Magnetic resonance imaging

C. Blanchard · T. Sliwa (✉) · Y. Voisin
Le2i, UMR 5158, Site Universitaire d'Auxerre,
Route des Plaines de l'Yonne, BP16, 89010 Auxerre, France
e-mail: sliwatadeusz@yahoo.fr

C. Blanchard
e-mail: cedric.blanchard@u-bourgogne.fr

Y. Voisin
e-mail: yvon.voisin@u-bourgogne.fr

A. Lalande · O. Bouchot
Le2i, UMR 5158, Faculté de Médecine, Université de Bourgogne,
7 Bld Jeanne d'Arc, BP 87900, 21079 Dijon, France
e-mail: alain.lalande@u-bourgogne.fr

O. Bouchot
e-mail: olivier.bouchot@chu-dijon.fr

Introduction

The aortic root comprises the annulus, the sinuses of Valsalva (SV), the aortic valve cusps (or leaflets), the commissures, the interleaflet triangles and the sino tubular junction (Fig. 1) [1,2]. The sinuses are named as right coronary sinus, left coronary sinus and the non coronary sinus respectively. Aortic valves are morphologically classified by the number of cusps as unicuspid, bicuspid or tricuspid aortic valves [3]. The bicuspid aortic valve is the most common congenital cardiac abnormality [4,5].

Grande et al. [6] have shown that the stress and strain due to physiologic pressure loading are highest in the non-coronary cusp and lowest in the left one. These differential results may explain the clinical incidence of isolated sinus dilatation.

Different pathologies could affect the aortic root and the most common one is the annulo ectasia disease. There is a risk of evolution towards aortic dissection with a high level of mortality. To avoid such an evolution, it is admitted that for a maximum diameter of the aorta of 50–55 mm, an aortic replacement is necessary [7].

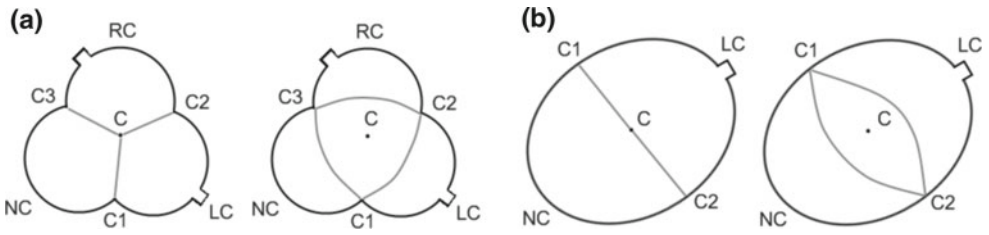

Fig. 1 Diastolic and systolic representations **a** of a tricuspid valve as visible on MR images, and **b** of a bicuspid valve with anterior-posterior cusps. RC, *right* coronary cusp; LC, *left* coronary cusp; NC, *noncoronary* cusp; C, *Centre* of the SV; C1, C2 and C3, commissures

For the past decade, with recent advanced techniques, the number of aortic valve surgical procedures has increased [8]. Recent data have shown that the prosthetic graft should incorporate the sinuses for proper valve closure. In order to share the stress with the cusps, the graft design must more closely resemble the original aorta [9]. Hence a global knowledge of the shape of the SV is required for the complete diagnosis or the design of a specific prosthesis.

However, there is no global consensus on the choice of methods for measuring aortic root dimensions. Although the transesophageal echocardiography of the aortic root is the commonly used preoperative tool [10,11], magnetic resonance imaging (MRI), and in particular cine-MRI, could be a well-suited technique since it has been shown to be useful in more precisely defining anatomy [12]. Indeed, the orientation of the plane in echocardiography does not ensure the measure of the maximal diameter, and for the SV, the measurement is considerably more difficult than for the sino-tubular junction or for the ascending aorta since the SV is not a cylindrical structure but a trifolied one.

In cine-MRI, the number of images usually acquired renders manual processing excessively time-consuming in clinical practice. A visual selection of the image with the maximum aortic surface and a manual determination of the maximum diameter could induce inter and intra-observer variations. To our knowledge, there is no method to automatically extract the contour of SV from MRI. In this paper, we propose a new method which automatically extracts and analyzes the SV shapes from cine-MRI without contrast material. The choice of a specific imaging plane that crosses the aortic root and the development of a robust, accurate and fast automatic post-processing method render our global protocol usable in clinical practice. This constitutes the first mandatory step towards a 3D representation of the aortic root from multiplane cine-MRI.

After the description of the data sets and of the imaging protocol, our automatic segmentation method based on geodesic reconstruction is detailed. The geodesic reconstruction was preferred to a more commonly used active contours approach, because the latter method is often slow, unpredictable and difficult to parameterize [13]. Geodesic reconstruction is a fast and simple method that can be controlled and corrected by means of mathematical morphology tools and statistical studies. The next step of our method consists in automatically detecting characteristic points and to then determine the different measures between the centre of the SV, the cusps and the commissures. Evaluation of our method was performed on synthesized data sets in order to find the limit conditions for the SV extraction, and on 41 patient data sets to determine the robustness of our whole method. The obtained values were compared with manual processing.

Methods

Synthesized data sets

Firstly, series of synthesized data sets have been built, including tricuspid SV, bicuspid SV and cylindrical SV prosthesis. Blur and noise are applied on images while the visibility of valve borders and the intensity of blood flow are also modified.

Each sequence is composed of 24 images. The isotropic spatial resolution is set to 1.6 mm per pixel, corresponding to the lowest resolution among our patient data base. The images cover a square of 80×80 mm and SV maximum diameter is set to 30 mm, whatever their morphology.

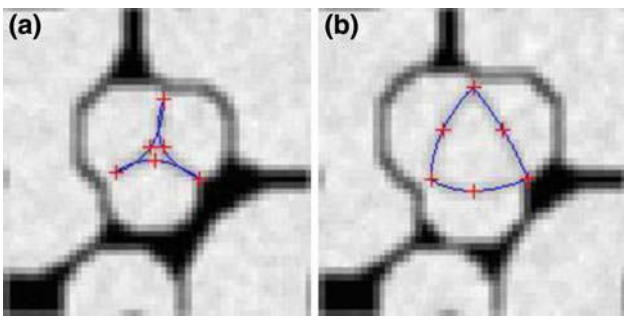

Fig. 2 Two images of a synthesized sequence. Three cubic splines (*in blue*) and their control points (*in red*) represent the cusps. **a** Image simulating the moment just after the diastole. **b** Image simulating the moment of the systolic phase

The SV shape is composed of one, two or three partially overlapping white disks. During a sequence, their positions vary slightly, simulating the evolution of the SV shape during a cardiac cycle. Some background shapes are added around the SV. In the SV, the edges of cusps can be represented as cubic valves starting and ending on commissures allowing the simulation of the movement of valves between diastole and systole (Fig. 2). For cylindrical SV prosthesis, the commissures are equidistant.

Simulation of flow intensity variations due to the blood flow are introduced by adding, in areas of high signal intensity, a random noise with low contrast C. Random intensity values are drawn from a standard uniform distribution on the open interval]1-C,1[. Moreover, when the signal-to-noise ratio (SNR) is greater than 3, the Rician noise present in MR images [14] tends towards a Gaussian distribution. Hence Gaussian blur and Gaussian noise can also be applied on each image.

To summarize, the intensity of valve shapes, blood flow contrast, noise and blur parameters are all customizable for each synthesized sequence. Some examples of synthesized images are presented in Fig. 3.

Subjects

Data were obtained from 41 patients with aortic root pathologies. Twenty-two patients had a SV dilatation (5 women, 17 men, age : 58 $\pm$ 13 years). Three further patients had a control examination after surgical procedure (3 men, ages: 61, 69 and 77 years). The surgical procedure was a valve sparing aortic root replacement for aortic insufficiency known as the reimplantation procedure (Tirone David procedure [15]), involving replacement of the aortic root without replacement of the aortic valve. The 16 remaining patient examinations concerned other pathologies associated with the aortic root (3 women, 13 men, age: 55 $\pm$ 18 years). Evaluation of the SV is included in a routine imaging protocol concerning the follow-up of aortic root diseases. The study was conducted in accordance with the recommendations of the local ethics committee. Twenty eight patients presented a tricuspid valve (25 with the native aortic root, and 3 with aortic root replacement with valve sparing (reimplantation procedure)). Four patients had a purely bicuspid valve, with no raphe and nine patients presented a bicuspid valve with one raphe (A raphe being defined as a line of fusion of two leaflets).

Image acquisition

Magnetic resonance imaging was performed on a 1.5 T magnetic resonance whole body imager (Siemens Magnetom Avanto, Siemens Medical Solution, Germany) using a phased array thoracic coil. The cine-MR images were acquired using a breath-hold ECG-gated steady-state free-precession sequence (TrueFISP sequence) with the following acquisition parameters: repetition time (TR) 1.54 ms, echo time (TE) 1.49 ms, 17 lines per segment, pulse flip angle (α) 65 degrees and a slice thickness of 5 mm. The temporal resolution was 27 ms per image. The in-plane isotropic spatial resolution varied from 0.7 mm per pixel to 1.6 mm per pixel, according to the patient examination (mean = 1.1 mm, standard deviation = 0.4 mm). From scout images orientated in the left ventricular long and short axes, acquisition according to the left ventricular outflow tract was performed (Fig. 4a). A second acquisition in the left ventricular outflow tract was performed, perpendicular to the first (Fig. 4b). The aortic valve cross-section was defined as the plane perpendicular to the two left ventricular outflow tract planes (Fig. 4c). Then, a series of cine MR images covering the whole cardiac cycle was acquired in this orientation.

Image processing

The automatic process involved three steps: the localization of the SV (Fig. 5) in each image, the detection of SV contours (Fig. 6) and the extraction of characteristic points (Fig. 7).

These points allow the metric evaluation of the SV. After a quick review of the useful tools of mathematical morphology, the different steps of our method are detailed in the following paragraphs.

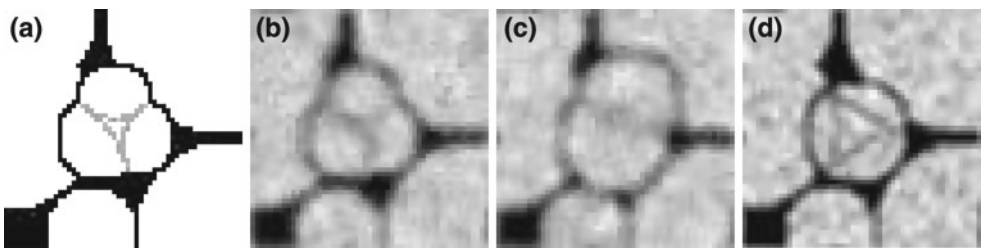

Fig. 3 For images from four synthesized sequences. **a** A tricuspid valve without noise or blur. **b** A blurred and noisy tricuspid valve. **c** A blurred and noisy bicuspid valve. **d** A blurred and noisy cylindrical SV prosthesis

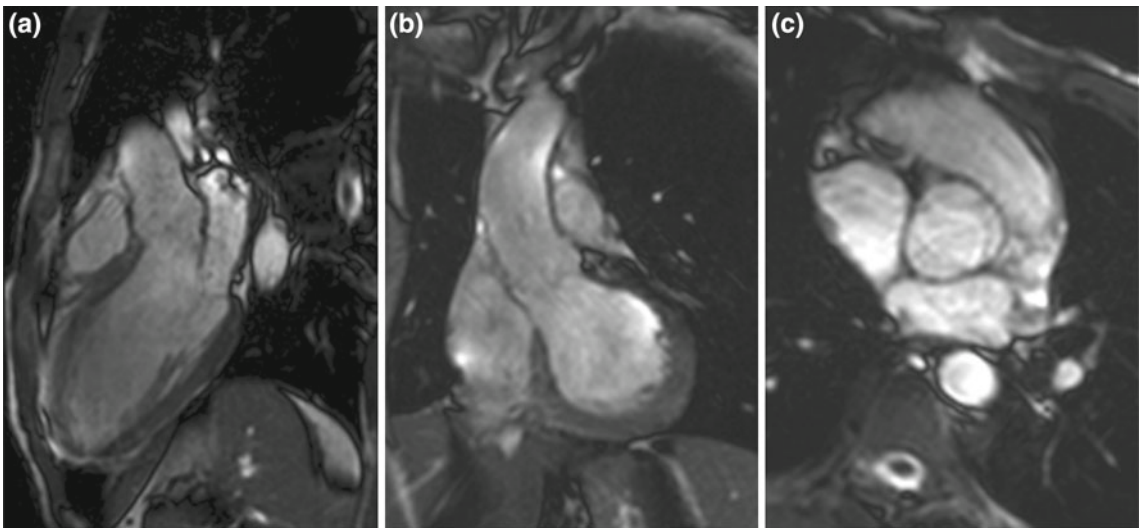

Fig. 4 Localization of the aortic valve cross-section plane. **a** *Left* ventricular outflow tract plane obtained from scout images. **b** *Left* ventricular outflow tract plane obtained perpendicularly from the precedent. **c** Aortic valve cross-section plane. This plane is perpendicular to the two *left* ventricular outflow tract planes

Mathematical morphology for image segmentation

The efficiency of mathematical morphology for image segmentation has already been demonstrated [16–18]. Some useful simple tools of greyscale morphology with flat structuring elements are presented here.

Let B_r be a disk of radius r, centred at the origin. B_r is an isotropic structuring element. The greyscale dilation (noted $\oplus$) of a function f by B_r is given by $g \oplus B_r(x) = \mathrm{Sup}\{g(x - y), y \in B_r\}$. Conversely, the greyscale erosion (noted $\ominus$) of f by B_r is given by $g \ominus B_r(x) = \mathrm{Inf}\{g(x - y), y \in B_r\}$. The composition of the erosion with the dilation (called opening) removes unwanted small components whereas the composition of the dilation with the erosion (called closing) erases the holes which are smaller than the structuring element.

The greyscale geodesic reconstruction [19] allows recovering an area from a marker. The reconstruction h of function f from g is the supremum of the geodesic dilations of g inside f (Fig. 8):

$$h = \mathrm{Sup}\{\mathrm{Inf}(g \oplus B_r, f), r > 0\}$$

Using this tool, one can fill holes in binary images, regardless of their sizes, by considering the geodesic reconstruction of the image border inside the set of pixels equal to zero.

An advantage of using mathematical morphology for image segmentation is that results are not very sensitive to small variations of parameters in a pipeline of morphological operations [17]. Hence these parameters can be coarsely chosen.

Localization of the SV

Let $I(k)$ be the frame number k. Firstly, a mask representing bright regions inside the body is extracted:

- We suppose that the whole body does not move during image acquisition. By means of a morphological closing and an erosion, the study area is restricted to within the body on $I(1)$ (Fig. 5b). The closing is performed using a big structuring element according to the common mean body size whereas the radius of the disk for the erosion relies on a visual estimation of the thickness of the fat around the body;
- Inside the body, a threshold equal to 30% of the maximum intensity is applied in order to keep visually bright pixels in each frame $I(k)$ (Fig. 5c). The set of bright pixels is called $A(k)$;
- The regularity of shapes is guaranteed by several morphological operations: holes are filled (by geodesic reconstruction), elements which are close to each other are merged by closing, small isolated elements are erased by opening (Fig. 5d);
- Finally, areas which are not in all frames are deleted by applying a constraint of temporal coherence (Fig. 5e).

Even if each region is not separately identified, the centre of each region can still be detected and the temporal movement of these centres are identified:

- For each image, the contours are detected inside the considered area by binarization of the norm of the gradient

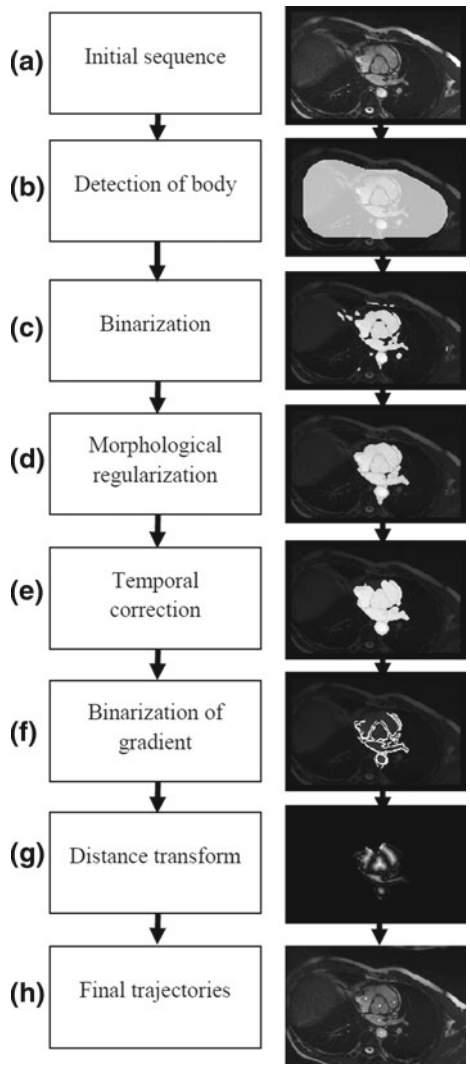

Fig. 5 Flow diagram summarizing the different steps of the localization of the SV. See text for complete explanation

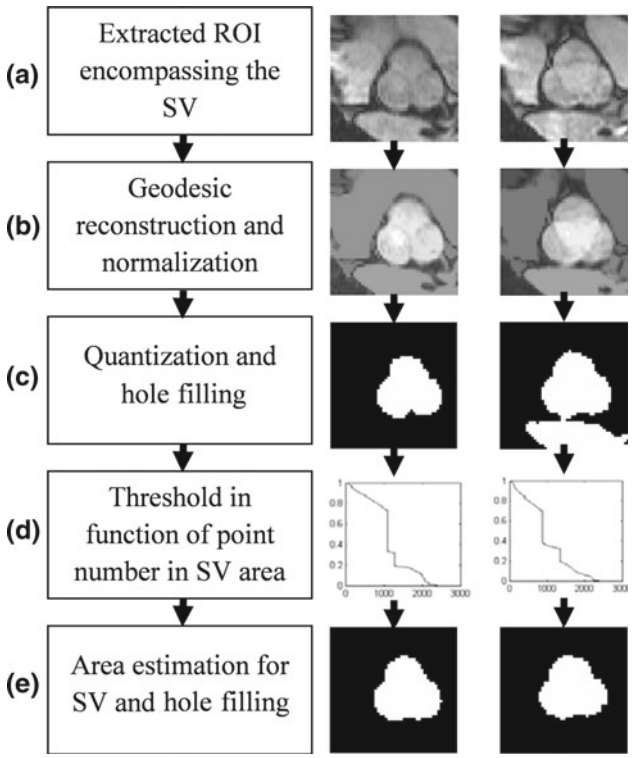

Fig. 6 Flow diagram summarizing the different steps of the extraction of the SV contours. Two examples from the same patient examination, the *left* one in diastole and the *right* one in systole, illustrate these different steps. See text for complete explanation

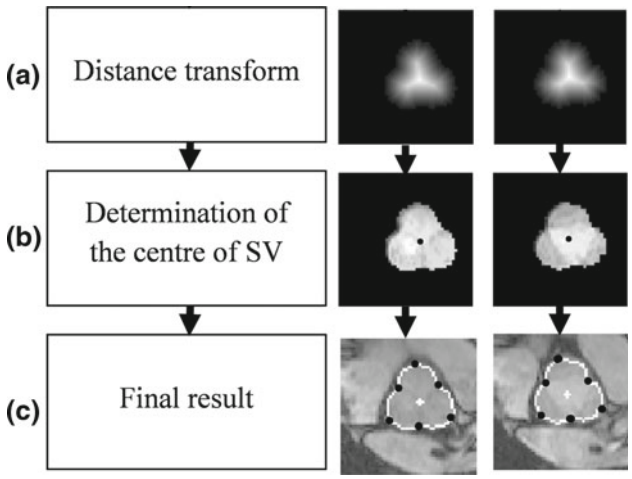

Fig. 7 Flow diagram summarizing the different steps of the extraction of relevant points. Two examples from the same patient examination, the *left* one in diastole and the *right* one in systole, illustrate these different steps. See text for complete explanation

with a threshold of 30% of the maximum norm. This constitutes the set G: $G(k) = \{\text{gradient}(I(k))/\max(\text{gradient}(I(k))) > 0.3\}$;

- In order to erase isolated significant gradients induced by noise and blood flow, we then make an erosion by a unit disk (in discrete space, a single pixel and its 4-connectivity neighbourhood) and a geodesic reconstruction inside G itself: $G' = \text{Sup}\{\text{Inf}((G \ominus B_1) \oplus B_r, G), r > 0\}$ (Fig. 5f);
- A distance map is computed using the Euclidean distance transform (i.e. the shortest distance is considered) (Fig. 5g) and local maxima are found inside bright regions (Fig. 5h);
- From these maxima, trajectory for each region is built by considering all the images of the sequence. A trajectory for a region is defined as a set of points, each point is located inside the region and there is one and only one point per frame;
- Finally, the user selects the trajectory of the SV on the first image of the sequence.

This trajectory allows the definition of a Region Of Interest (ROI) which includes the SV in each frame of the sequence (Fig. 6a). The size of the ROI is automatically set to 80 mm (the number of considered pixels varies according to the pixel spacing) since it empirically fits with all SV sizes of the patient data sets.

Estimation of the SV area

During a cardiac cycle, the variation of the sinus surface will not exceed certain limits. Indeed, an area variation of about 20% is a maximum physiologically acceptable variation of the SV area during a cardiac cycle [20] and SV area is often almost constant. Hence the mean area value is determined by the following step in order to control the extraction of SV contours:

- Since the centre of the extracted ROI is always inside the SV, a geodesic reconstruction is performed on the ROI (Fig. 6b) from the 8-connectivity neighbourhood of the ROI centre in order to recover the SV shape from this marker. As a consequence, high grey scale intensities outside the centred region disappear (Fig. 8b).
- Then, each image is binarized by Minimum Variance Quantization (MVQ) [21] and holes are filled (Fig. 6c) because SV shapes are theoretically simply connected. However, although MVQ often provides good thresholds automatically, this method sometimes fails when the geodesic reconstruction does not provide a significant intensity difference between the SV area and other areas. This is mainly due to a partial volume effect produced by the relative thinness of the SV edge.
- On each binarized image, the area is computed by simply summing white pixels. Let $A_{\min}$ be the minimum of area values. $A_{\min}$ constitutes the minimal acceptable area and is a reliable first estimation of SV area even if there may be an underestimation. Conversely the maximum of area values is not a pertinent supremum because huge overestimations due to ambiguous junctions could be present. So, a maximal acceptable area ($A_{\max}$) is defined as $1.5 \times A_{\min}$ and only areas under $A_{\max}$ are kept. Thus the greatest values from images are not retained when the MVQ binarization fails due to ambiguous junctions.
- Subsequently, the mean (m) and the standard deviation (σ) of remaining values are calculated. The most incoherent cases are eliminated providing a robust mean value of the SV area. Indeed, the set of area values can be seen as an independent random variable for which the probability of being in the interval $[m-3\sigma, m+3\sigma]$ is almost 99.7%. Only the values that are in this interval are kept, the mean and the standard deviation of the new set are computed and the selection is repeated three times (in our case, four iterations or more gave no significant improvements). The final mean (m) provides the reference area corresponding to sinuses.

Extraction of the SV contours

In order to extract the SV edges, the result of geodesic reconstruction is binarized a second time using the mean area (m) to automatically choose the correct threshold for each image.

To be more precise, a cumulative histogram from highest to lowest intensities (Fig. 6d) is computed on the ROI of each image. Indeed it gives information about the number of points with intensity greater than a certain value. When the threshold decreases from 1 to 0, this number increases from 0 to the total number of points. The required threshold is obtained directly from each curve by determining the level for which the number of points is the nearest to the mean area (m).

Examples in Fig. 6e represent the resultant image after the application of a threshold, followed by filling holes as previously and a morphological closing to regularize the contours. The ambiguous junction shown in Fig. 5d is corrected.

Furthermore, if the absolute difference between the mean area of the whole sequence (m) and the SV estimated area on one frame exceeds 20% of the mean (m), the corresponding frame is classified as a recalcitrant case and is removed from the sequence.

Determination of characteristic points

The last part of our process aims to detect relevant points such as SV centre, commissures and cusps and to give measurements between these points:

- The centre of the SV region is defined as the centre of the maximum disk surrounding the lumen whatever its shape (tricuspid or bicuspid valves). This definition avoids the problems associated with the barycentre location of complex shapes. Moreover, this disk matches perfectly the geometric centre in the case of a cylindrical prosthesis. The position of the SV was estimated in the first step of our process, but to more precisely determine this centre, the Euclidean distance transform is now applied on the complimentary of the SV region (Fig. 7a). Candidate points are pixels having the greatest distance. If more than one candidate point is found, the barycentre of these points is taken. On the examples in the Figs. 7b and 9a, this centre falls within the movement area of valve cusps.
- For each cusp, radii are defined as the Euclidian distance between the centre of the SV region and the border pixels of the SV. To estimate the geometrical properties of the SV, the local maxima and minima of radii are then

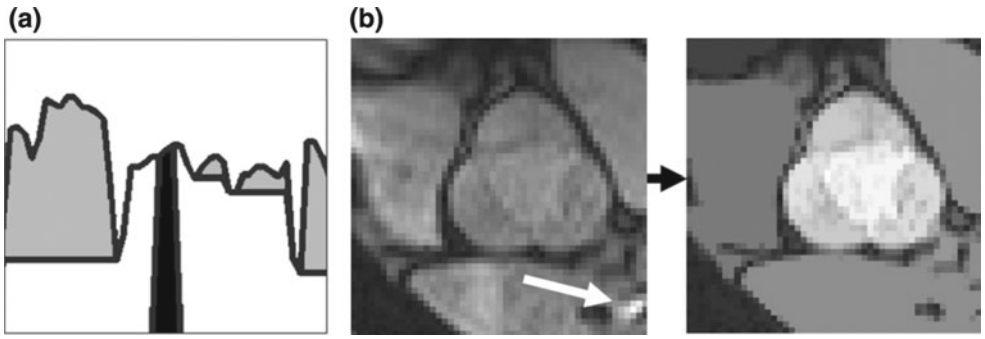

Fig. 8 **a** Geodesic reconstruction (*in white*) of f (*in gray*) from g (*in black*). **b** Example of geodesic reconstruction of a diastolic image. The hypersignal shown by the white arrow is eliminated

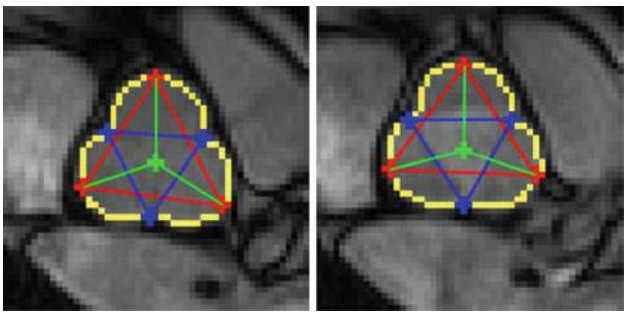

Fig. 9 Example on diastolic and systolic images of automatic processing for a tricuspid valve and graphic representation of the measures. SV contours are in *yellow*, distances between each cusp to the centre in *green*, distances between two commissures in *blue* and distances between two cusps in *red*. The distances between each cusp to the opposite commissure are not displayed

located in each frame. As each cusp must have only one maximum, indifferently for tricuspid (three local maxima) and bicuspid valves (two local maxima), maxima positions cannot be close to each other. So, a constraint concerning the minimal distance of separation between these maxima is added. The radius (R) of a disk of same area as the SV region is an usable threshold for this condition whatever the size and the shape of the SV. From all local maxima, only those having the highest value in a distance of R are kept. Moreover if there are n different local maxima $P_1, .., P_n$ with the same radius and $|P_i, P_j| \leq R$ for all $(i, j) \in [1, n]$, the median position along the edge is kept as the location of the local maximum.

- Similarly, the commissures are obtained from minimum distances from centre to border (Fig. 7c). An example of final results is shown in Fig. 9b.

Measurement of the relevant distances

A reliable estimation of radii is obtained using the same processing as for the area estimation (three consecutive selections in the interval $[m - 3\sigma, m + 3\sigma]$). The mean number of radii (m_r) per image in the sequence determines the classification of sinus as bicuspid or tricuspid (in our automatic classification, a tricuspid valve with a raphe is classified as tricuspid).

With knowledge of the spatial resolution, the different distances can then be calculated. In the case of tricuspid valves (and by extension in the case of bicuspid valve with a raphe), the considered points are detailed in the Fig. 1a. The considered points for a bicuspid valve case are detailed in the Fig. 1b. The calculated distances from these marks are to the distances between each cusp to the centre of the SV, the distances between each cusp to the opposite commissure, the distances between two commissures and finally to the distances between two cusps.

The image with the maximal sum (respectively minimal sum) of the distances of each cusp to the centre of the SV is considered as the systolic (respectively diastolic) image (Fig. 7c).

Evaluation of the method

The SV extraction was initially tested on the synthesized data sets. Then, for each patient, the automatic measurements on all the images were compared with manual measurements performed on diastolic and systolic images that had been visually selected. The results obtained with manual tracing were considered as the reference measures. For the inter-observer variation study, manual measurements were performed independently by two experienced observers on ten specific cases (seven patients with tricuspid valves, one with a bicuspid valve, one with a biscuspid valve with a raphe and one with prosthesis on tricuspid valve). An intra-observer variation study was performed on the same patient data set. For the intra-observer variation study the results obtained with the first manual tracing were considered as the reference measures. The comparisons were performed with a linear regression analysis. In addition, the agreement between methods was verified using the Bland–Altman method [22]. The Bland–Altman plot was generated by considering the

Table 1 Limit conditions for a correct extraction of SV edges from synthetic data

MRI Gaussian noise SD	MRI Gaussian blur		Blood noise contrast (%)	Valve intensity (%)
	Filter size (px)	SD		
No	No	No	No	<95
No	No	No	60	<40
No	9	1.5	60	<50
No	9	<2.2	60	No
No	5	<2.6	60	40
0.01	5	<2.2	60	40

In the first three cases, valve intensities (in % of the maximum intensity value) vary while other parameters were constant during the tests. In the other three cases, the standard deviation of the Gaussian blur varies while other parameters remain constant. Blood noise contrast is expressed in % of the maximum intensity value

measurements obtained with the manual tracing as the independent variable and the corresponding values obtained with automatic processing as the dependant variable. Statistical differences between groups were compared with the paired t-test. $P < 0.05$ was considered to indicate a statistically significant difference.

Firstly, all the measures in diastole (respectively in systole) were considered together. Secondly, four specific groups with homogeneous data were considered: the distances between each cusp to the centre of the SV, the distances between each cusp to the opposite commissure, the distances between two commissures and the distances between two cusps. Bland–Altman evaluations were performed on each of these groups. Hence the accuracy of cusp or commissure detections can be assessed.

Results

Synthesized data sets

Tricuspid SV are correctly extracted and there is at most one rejected image under the various conditions presented in Table 1. The intensity of the valve edge must not be too important, otherwise the geodesic reconstruction is too heavily influenced by its presence. Fortunately, the reconstruction is more flexible if the image is blurred. Gaussian noise can also influence the success of our extraction as shown in the two last cases in Table 1. Under these conditions, we are visually close to poor conditions.

Results are almost the same for bicuspid SV and cylindrical SV prosthesis. Figure 3 shows some examples of synthesized data sets where SV are correctly extracted. All these tests show that our automatic extraction works correctly under various conditions and specific MR resolution but can fail or reject some frames if the image quality is too close or lower than the empirically found limit conditions. Moreover, the cylindrical SV prosthesis is the hardest shape to evaluate since its cusps and its commissures have the same radii. In this case, the valve edges must be visible enough to produce a small notch in the cylindrical boundaries of SV. Inversely, valve edges must not be too visible since it can influence too heavily the geodesic reconstruction and its binarization.

Patient data sets

On the 41 patient examinations, 30 sequences have no recalcitrant image and only 5.0% of the whole set of images are classified as recalcitrant cases and are rejected due to failure of the segmentation.

Figures 9 and 10 illustrate two examples of post-processing on tricuspid valve cases. In Fig. 10a, some images have poor segmentation at the MVQ step. They are corrected by ensuing steps, providing appropriate results (Fig. 10b). Figure 11 illustrates an example of correct classification of a bicuspid aortic valve. In Fig. 11a, many images with poor segmentation are corrected by the following steps. The second image is even eliminated. The last statistical estimation step is necessary to correct some imperfect point detections as shown in Fig. 11b. For example, the third image has an ill-positioned red point. With the recursive statistical estimation, these cases are not taken into account for the final measures and classification. Figure 12 illustrates the case of post-processing on a bicuspid aortic valve with a false raphe. This case is classified as tricuspid. This result is considered as correct because a bicuspid valve with a false raphe includes three cusps. The example shown in Fig. 13 is the case of a tricuspid prosthesis valve, with a number of difficulties due to the shape of the prosthesis. Although the shape of the valve is awkward to manage, because it is close to a circular shape, the algorithm provides good results and classifies the sinuses as tricuspid. This classification is correct, because surgery with Tirone David procedure preserved the initial tricuspid valve.

Numerical results

Concerning the intra-observer variation study, there is an excellent correlation ($r = 0.99$; $y = x + 0.24$; $P < 10^{-5}$) and an excellent agreement between the two manual processing procedures (mean value of the differences = 0.4 mm; standard deviation of the differences = 1.4 mm). Moreover, concerning the inter-observer variation study, there is an excellent correlation ($r = 0.98$; $y = 0.94x + 1.21$; $P < 10^{-5}$) and an excellent agreement between the two manual processing procedures (mean value of the differences = 0.7 mm; standard deviation of the differences = 1.9 mm).

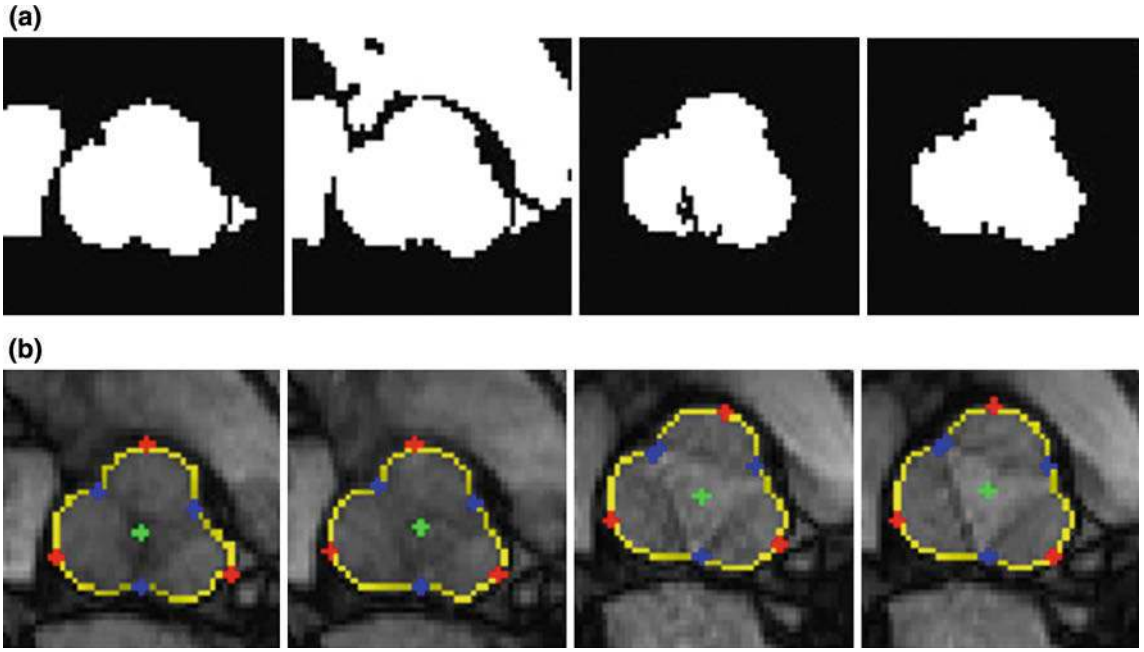

Fig. 10 Four examples extracted from a sequence containing a tricuspid valve. **a** First binarization of the geodesic reconstruction. **b** Automatically extracted SV contour and relevant points

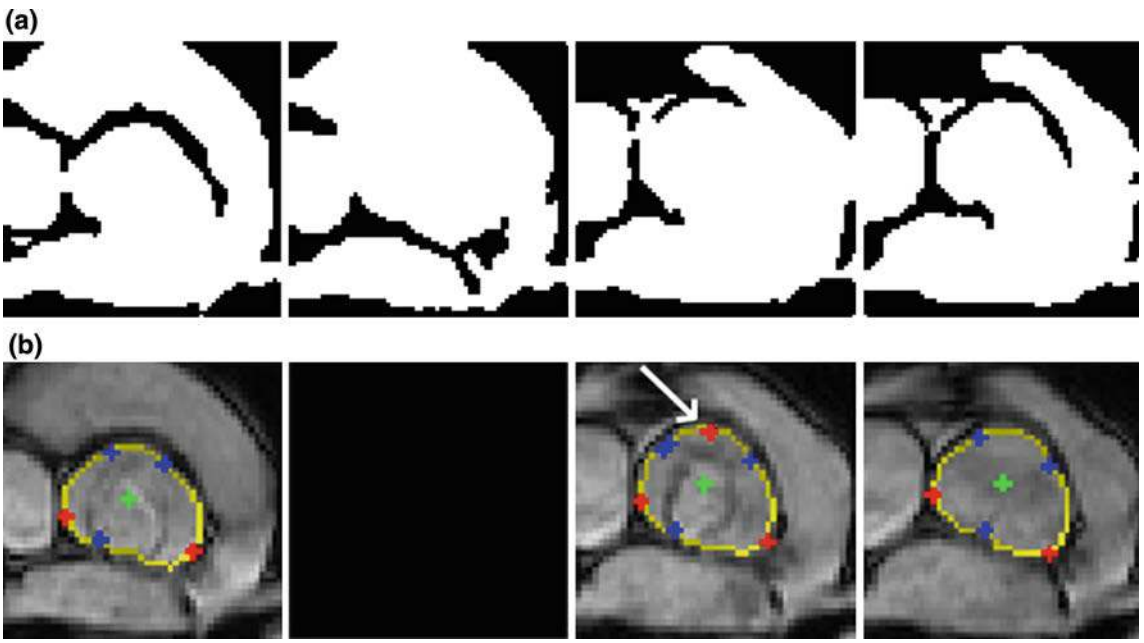

Fig. 11 Four examples extracted from a sequence containing a bicuspid valve. **a** First binarization of the geodesic reconstruction. **b** Automatically extracted SV contour and relevant points. The second image has been eliminated by the method and the third one contains a false cusp point which will not be take into account for measurements

Considering the entire set of measurements, there is an excellent correlation between manual and automatic measurements for both the diastole ($r = 0.97$; $y = 0.97x + 0.57$; $P < 10^{-5}$; Fig. 14a) and the systole ($r = 0.96$; $y = 0.96x + 1.2$; $P < 10^{-5}$; Fig. 15a) phases. The corresponding Bland–Altman plots are presented in Figs. 14b and 15b. For the diastole, the mean value of the differences is equal to -0.2 mm and the standard deviation is equal to 2.0 mm. For the systole, the mean value of the differences is less than 0.1 mm and the standard deviation is equal to 2.4 mm. These values show that

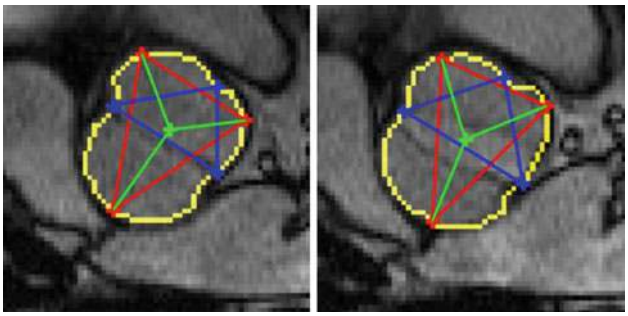

Fig. 12 Example of automatic processing for a bicuspid valve with a raphe. See legend of Fig. 9 for more explanations

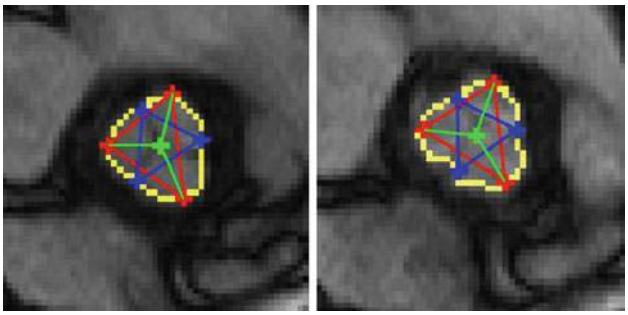

Fig. 13 Example of automatic processing for a patient with a prosthesis. See legend of Fig. 9 for more explanations

there is no bias between the automatic method versus manual tracing. By comparing these values with the image pixel size, we can conclude that these results are excellent. The Table 2 provides the Bland–Altman estimations according to homogeneous clusters. Whatever the distances, the mean of differences is smaller than the image pixel size, in both diastole and systole.

Discussion

The long-term survival of patients who have undergone aortic root surgery depends on different factors such as the surgical technique. The development of new techniques requires more precise information on the anatomy of the aortic valve structure. Today, there is no consensus on the method allowing geometric modelling of functional aortic valves for individual patient. A first step would be to define a reliable imaging modality, in order to perform an accurate morphometric study.

Using cross-sectional cine-MRI, Burman et al. [23] have manually measured the cusp-cusp and cusp-commissure dimensions at maximum systolic distension and at end-diastole. In our opinion, a choice must be made between these two distances and the distance between cusps and the centre. Indeed, the detection of the centre of the aortic valve enables the measure of each cusp separately, and hence allows a study

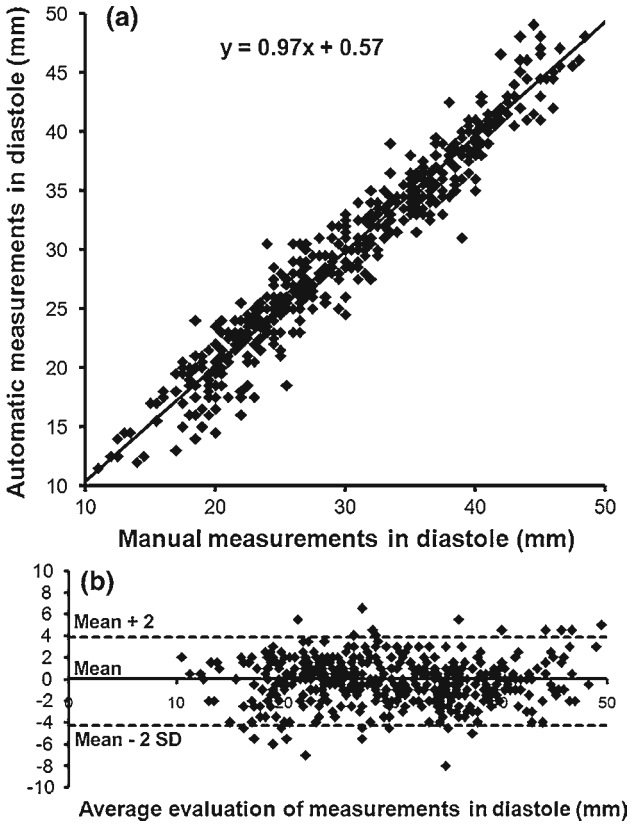

Fig. 14 Comparison between manual and automatic measurements for the diastolic images of the 41 patient examinations. **a** Correlation between the measurements of the different distances obtained with a manual tracing and the automatic processing. **b** The corresponding Bland–Altman plot

of aortic root asymmetry as well as the detection of isolated dilatation of one cusp.

In this article, an automatic segmentation method was used to measure the SV. MR imaging techniques appear to be particularly attractive for the study of the aortic root, allowing direct and non-invasive measurement of SV. The use of a SSFP-type sequence provides high spatial and temporal resolution images, as well as an excellent contrast between the blood and the tissues. Acquisition during breathhold allows one to deal with the artefacts due to diaphragmatic motion. The chosen plane allows the distance measurements between cusps, commissures and the centre of the aorta without partial volume effects. Contrary to echocardiography, the aortic root asymmetry can be studied.

The estimation of SV area on the whole sequence improves the robustness of the segmentation, in particular, due to the $A_{\max}$ threshold that removes incorrect cases. Moreover, the definition of the centre of the SV is based on a transformation distance map, which is more efficient than a classical barycentre location. Finally, the method of location of the different relevant points includes a module for the elimination of the non-realistic cases. The present study

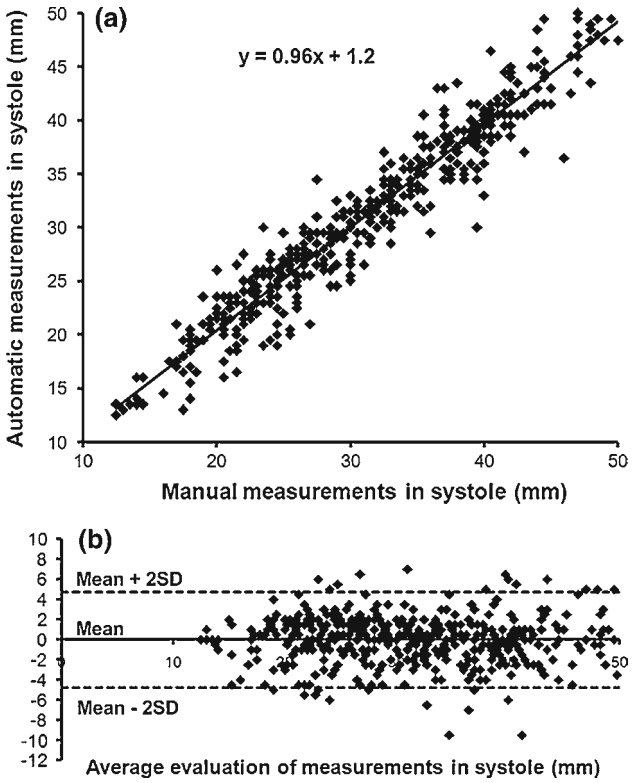

Fig. 15 Comparison between manual and automatic measurements for the systolic images of the 41 patient examinations. **a** Correlation between the measurements of the different distances obtained with a manual tracing and the automatic processing. **b** The corresponding Bland–Altman plot

Table 2 Comparison between manual and automatic processing on the 41 patient examinations

	Diastole		Systole	
	Mean	SD	Mean	SD
Cusp–cusp distances	−0.6	2.2	−0.5	3.0
Cusp–centre distances	0.7	1.5	0.9	1.9
Commissure–commissure distances	0.0	3.3	0.2	3.6
Cusp–commissure distances	−1.1	3.1	−0.4	4.4

Mean and standard deviation (SD) of differences between manual and automatic processing (in mm) using Bland–Altmann method by grouping the measures in homogeneous clusters

shows that our shape evaluation can be an efficient alternative to manual measurement or the use of active contours algorithms. Compared with these classical tools, our method is quick and uses simple parameterization. Even if the parameters of morphological operations can be coarsely chosen, the quality of results obviously depends on the MR-imaging sequence, the acquisition parameters, the success of each step of the method and the choice of thresholds.

The method was tested on 41 patient examinations by considering the distance measures between relevant points obtained for the diastolic and systolic phases. Globally, the measures obtained automatically are close to the manual ones and there is no bias between the automatic method and the manual tracing. In general, the differences are due to the definition of the boundaries in the geodesic reconstruction and the small size of SV in terms of pixels. The relative differences are greater for the distances with the commissure points than for the distances calculated with the cusp points. Indeed, as the commissure points are singular points (contrary to cusp points that are located on an area without an important variation of radius), a small difference in the location of these points causes a larger difference in the involved measures of distance (contrary to cusp points that neighbour pixels and produce the same distances).

The use of MR data acquired from one specific plane also has its limits. Indeed, the aortic root changes position during the heart contraction and the through-plane motion could be important [24]. Our work is the first essential step towards a 3D representation of the aortic root from several acquisitions covering the whole aortic root, from the annulus to the sinotubular junction. Moreover, even when considering only one plane, acquiring the whole cardiac cycle allows us to get the SV maximum diameter, in spite of the through-plane motion.

Conclusions

In conclusion, the reliable morphometric evaluation of the SV is crucial in the follow up of patients with aortic root pathologies, and by extension to the surgery indication. Cine-MRI in a cross-sectional orientation seems to be an attractive modality, but currently, there is no consensus on the measured distance in this orientation. We propose an original automatic method providing several reference measures, based on the automatic location of the centre of the SV, and on the commissure and the cusp positions. This method uses mathematical morphology combining numerical geodesic reconstruction with area estimation and distance transform function. Application of this method on typical patient examination cases provides results close to those obtained with a manual evaluation. Future works are the segmentation and analyse of the SV from multiplane sequences and then the building of a 3D representation of them. Then, the automatic evaluation of the SV will be applied on more patient examinations, in particular on a healthy population or on a patient population having the same pathology, in order to discuss the current reference values of measurement in terms of pertinence or accuracy.

Acknowledgments The authors would like to thank Dr Paul M. Walker for his precious help in the redaction of this article. They would also like to thank the regional council of Burgundy and the city of Auxerre for supporting this work.

References

1. Underwood MJ, El Khoury G, Deronck D, Glineur D, Dion R (2000) The aortic root: structure, function, and surgical reconstruction. Heart 83(4):376–380
2. Anderson RH (1997) Coronary arteries arising from the contralateral aortic sinus: electron beam computed tomographic demonstration of the initial course of the artery with respect to the aorta and the right ventricular outflow tract. J Thorac Cardiovasc Surg 113(5):961–962
3. Sievers HH, Schmidtke C (2007) A classification system for the bicuspid aortic valve from 304 surgical specimens. J Thorac Cardiovasc Surg 133(5):1226–1233
4. Roberts WC (1970) The congenitally bicuspid aortic valve: a study of 85 autopsy cases. Am J Cardiol 26(1):72–83
5. Peterson MD, Roach RM, Edwards JE (1985) Types of aortic stenosis in surgically removed valves. Arch Pathol Lab Med 109(9):829–832
6. Grande KJ, Cochran RP, Reinhall PG, Kunzelman KS (1998) Stress variations in the human aortic root and valve: the role of anatomic asymmetry. Ann Biomed Eng 26(4):534–545
7. Patel HJ, Deeb GM (2008) Ascending and arch aorta: pathology, natural history, and treatment. Circulation 118(2):188
8. Albes JM, Stock UA, Hartrumpf M (2005) Restitution of the aortic valve: what is new, what is proven, and what is obsolete. Ann Thorac Surg 80(4):1540–1549
9. Kunzelman KS, Grande KJ, David TE, Cochran RP, Verrier ED (1994) Aortic root and valve relationships: impact on surgical repair. J Thorac Cardiovasc Surg 107(1):162–170
10. Vasan RS, Larson MG, Levy D (1995) Determinants of echocardiographic aortic root size: the Framingham Heart Study. Circulation 91(3):734–740
11. Roman MJ, Devereux RB, Kramer-Fox R, O'Loughlin J (1989) Two-dimensional echocardiographic aortic root dimensions in normal children and adults. Am J Cardiol 64:507–512
12. Feldman DN, Roman MJ (2006) Aneurysms of the sinuses of Valsalva. Cardiology 106(2):73–81
13. Acton S, Ray N (2009) Biomedical image analysis: segmentation. Synth Lect Image Video Multimed Process 4(1):1–108
14. Gudbjartsson H, Patz S (1995) The Rician distribution of noisy MRI data. Magn Reson Med 34(6):910–914
15. David TE (2002) Aortic valve sparing operations. Ann Thorac Surg 73(4):1029–1030
16. Soille P (2004) Morphological image analysis: principles and applications, 2nd edn. Springer, Berlin
17. Serra J (2006) A lattice approach to image segmentation. JMIV 24(1):83–130
18. Salembier P, Serra J (1995) Flat zones filtering, connected operators, and filters by reconstruction. IEEE Trans Image Process 4(8):1153–1160
19. Vincent L (1993) Morphological grayscale reconstruction in image analysis: applications and efficient algorithms. IEEE Trans Image Process 2(2):176–201
20. Lansac E, Lim HS, Shomura Y, Lim KH, Rice NT, Goetz W, Acar C, Duran CM (2002) A four-dimensional study of the aortic root dynamics. Eur J Cardiothorac Surg 22(4):497–503
21. Wu X (1991) Efficient statistical computations for optimal color quantization. In: Arvo J (ed) Graphics gems II. Academic Press, London, pp 126–133
22. Bland JM, Altman DG (1986) Statistical methods for assessing agreement between two methods of clinical measurement. Lancet 8:307–310
23. Burman ED, Keegan J, Kilner PJ (2008) Aortic root measurement by cardiovascular magnetic resonance: specification of planes and lines of measurement and corresponding normal values. Circ Cardiovasc Imaging 1:104–113
24. Kozerke S, Scheidegger MB, Pedersen EM, Boesiger P (1999) Heart motion adapted cine phase-contrast flow measurements through the aortic valve. Magn Reson Med 42(5):970–978